Independent Evaluation of the Ability of Spaceborne Radar and Lidar to Retrieve the Microphysical and Radiative Properties of Ice Clouds

ROBIN J. HOGAN,* DAVID P. DONOVAN,+ CLAIRE TINEL,#,& MALCOLM E. BROOKS,*,** DOMINIQUE BOUNIOL,# ANTHONY J. ILLINGWORTH,* AND J. PEDRO V. POIARES BAPTISTA@

*Department of Meteorology, University of Reading, Reading, United Kingdom
+ Royal Dutch Meteorological Institute, De Bilt, Netherlands
# Centre d'Étude des Environnements Terrestre et Planétaires, Institut Pierre Simon Laplace, Paris, France
@ European Space Agency, Noordwijk, Netherlands

(Manuscript received 6 October 2004, in final form 16 March 2005)

ABSTRACT

The combination of radar and lidar in space offers the unique potential to retrieve vertical profiles of ice water content and particle size globally, and two algorithms developed recently claim to have overcome the principal difficulty with this approach—that of correcting the lidar signal for extinction. In this paper "blind tests" of these algorithms are carried out, using realistic 94-GHz radar and 355-nm lidar backscatter profiles simulated from aircraft-measured size spectra, and including the effects of molecular scattering, multiple scattering, and instrument noise. Radiation calculations are performed on the true and retrieved microphysical profiles to estimate the accuracy with which radiative flux profiles could be inferred remotely. It is found that the visible extinction profile can be retrieved independent of assumptions on the nature of the size distribution, the habit of the particles, the mean extinction-to-backscatter ratio, or errors in instrument calibration. Local errors in retrieved extinction can occur in proportion to local fluctuations in the extinction-to-backscatter ratio, but down to 400 m above the height of the lowest lidar return, optical depth is typically retrieved to better than 0.2. Retrieval uncertainties are greater at the far end of the profile, and errors in total optical depth can exceed 1, which changes the shortwave radiative effect of the cloud by around 20%. Longwave fluxes are much less sensitive to errors in total optical depth, and may generally be calculated to better than 2 W m^{-2} throughout the profile. It is important for retrieval algorithms to account for the effects of lidar multiple scattering, because if this is neglected, then optical depth is underestimated by approximately 35%, resulting in cloud radiative effects being underestimated by around 30% in the shortwave and 15% in the longwave. Unlike the extinction coefficient, the inferred ice water content and particle size can vary by 30%, depending on the assumed mass–size relationship (a problem common to all remote retrieval algorithms). However, radiative fluxes are almost completely determined by the extinction profile, and if this is correct, then errors in these other parameters have only a small effect in the shortwave (around 6%, compared to that of clear sky) and a negligible effect in the longwave.

1. Introduction

Ice clouds play an important role in the radiation budget of the earth (Liou 1986), but the global, vertically resolved observations necessary to evaluate their representation in climate models are lacking. Brown et al. (1995) estimated that spaceborne 94-GHz radar should be able to retrieve ice water content (IWC) to within a factor of 2, reducing to around ±40% if additional information were available on particle size. The combination of radar and lidar has the potential to yield accurate size measurements due to the large difference in the size dependence of the backscatter. Such measurements will shortly be available with the launch of the CloudSat radar and the Calipso lidar (Stephens et al. 2002), and later this decade with the Earth Cloud, Aerosol and Radiation Explorer (EarthCARE) mission, involving a cloud radar and lidar on the same platform (European Space Agency 2004).

& Current affiliation: Centre National d'Etudes Spatiales, Toulouse, France.
** Current affiliation: Met Office, Exeter, United Kingdom.

Corresponding author address: Robin J. Hogan, Department of Meteorology, Earley Gate, P.O. Box 243, Reading RG6 6BB, United Kingdom.
E-mail: r.j.hogan@reading.ac.uk

Intrieri et al. (1993), Mace et al. (1998), and Wang and Sassen (2002) have combined ground-based radar and lidar to derive the properties of ice clouds, but a problem that arises in more optically thick clouds is extinction of the lidar signal. Attempting to correct the lidar for extinction by simply assuming a relationship between backscatter and extinction is problematic because small changes in the relationship yield rapidly diverging extinction profiles, and from the lidar alone there is insufficient information to choose between them (except in the special case that the lidar detects the molecular return at the far side of the cloud). A solution is to make use of the radar information in the extinction-correction stage, because only a very small range of these possible extinction profiles yields plausible profiles of particle size or number concentration when combined with the radar. This idea has led to the development of two different algorithms, one by Donovan and van Lammeren (2001) [hereafter the "Koninklijk Nederlands Meteorologisch Instituut (KNMI) algorithm"] and the other by Tinel et al. (2005) [hereafter the "Institut Pierre-Simon Laplace (IPSL) algorithm"]. The first has been run successfully on large volumes of ground-based data (e.g., Donovan 2003), but from space it will be possible to apply them to a far greater fraction of ice clouds due to the absence of intervening liquid water clouds (Hogan et al. 2004).

The purpose of this paper is to assess the skill of the two algorithms in retrieving profiles of the IWC, visible extinction coefficient (α), and effective radius (r_e) in ice clouds, assuming that mixed-phase clouds can be identified and excluded from consideration using the lidar polarization capability. The parameters of interest are not independent, being linked by (Foot 1988)

$$r_e = \frac{3}{2}\frac{\mathrm{IWC}}{\rho_i \alpha}, \tag{1}$$

where ρ_i is the density of solid ice. The visible extinction coefficient is the most important parameter for determining the radiative properties of the cloud in the short wave, and for particles of radius greater than around 30 μm it is closely linked to the properties in the longwave, because geometric optics then applies in both regions of the spectrum. It is also the parameter that can be most accurately determined from the combination of lidar and radar. Numerical models, however, usually hold ice water mixing ratio as a prognostic variable, and must parameterize r_e in order to obtain α for radiation calculations.

Independent evaluation of the algorithms is achieved by means of "blind tests"; one of the authors (RJH) used ice size distributions measured during aircraft descents through midlatitude frontal clouds to generate the radar and lidar backscatter profiles that would be measured from space. These were provided to the authors of the two algorithms (DPD and CT) who applied their codes with no knowledge of the original measurements and only limited knowledge of the assumptions that had been made in the synthesis of the profiles. The retrieved IWC, α, and r_e were then compared to the "true" values. Finally, 1D radiation calculations were performed (by MEB) to determine the impact of any errors in the retrievals on the longwave and shortwave flux profiles.

The instrument characteristics of the proposed EarthCARE satellite were used in simulating the profiles, although the results are also applicable to the CloudSat/Calipso satellites as well as ground-based systems. We consider only the simple elastic backscatter of the lidar; neither polarization capability nor the high spectral resolution of EarthCARE are included in the simulation.

Two blind tests were performed, each consisting of five profiles. In the first, the instruments were assumed to be noise free and almost infinitely sensitive, and the lidar extinction-to-backscatter ratio S was allowed to vary by as much as a factor of 2 within each profile (with the algorithms having no information about the nature of S). In this way the ability of the algorithms to recover extinction in clouds with a one-way optical depth as much as 7 was evaluated. Their success prompted a more realistic second blind test, in which instrument noise was added to a new set of profiles, along with the effects of lidar multiple and molecular scattering.

In section 2 the principles behind the two algorithms are outlined. The generation of the profiles from aircraft data is described in section 3, and in section 4 the results of the two blind tests are analyzed in terms of the sensitivity of the retrievals to a number of factors. The impacts of retrieval errors for the implied radiative properties of the clouds are reported in section 5.

2. Description of the algorithms

a. Theoretical background

The principle behind radar–lidar retrievals of cloud properties is straightforward: radar measures reflectivity factor Z, approximately proportional to the sixth power of particle size, while the lidar return is related to particle size to the power two. Therefore, the ratio of the two is proportional to the fourth power of size, enabling size to be retrieved very accurately. With a suitable assumption on the nature of the size distribution (such as it being a gamma distribution of a particu-

lar order), other moments of the distribution (such as water content) and measures of size (such as r_e) may be estimated.

O'Connor et al. (2005) recently took this approach to retrieve the parameters of drizzle falling beneath stratocumulus. The scattering properties of liquid droplets can be calculated accurately, enabling the measurements to be interpreted unambiguously, but things are more uncertain in ice clouds due to the multitude of particle habits that can occur. The radar reflectivity factor of ice clouds is usually expressed assuming the particles to be spheres of diameter D consisting of a homogeneous mixture of ice and air with a density that varies with D alone (e.g., Brown et al. 1995):

$$Z = \frac{1}{0.93}\int_0^\infty n(D)|K(D)|^2 D^6 \gamma(D)\, dD, \tag{2}$$

where $n(D)dD$ is the number concentration of particles with diameter between D and $D + dD$, $|K|^2$ is the dielectric factor (proportional to density squared), and γ is the Mie-to-Rayleigh backscatter ratio. In reality ice particles are not spheres and a simple density relationship is not strictly applicable to all the sampled particles, so this may be generalized to a summation over volume V of particles of arbitrary habit (Hogan et al. 2006):

$$Z = \frac{|K_i|^2}{0.93}\left(\frac{6}{\pi\rho_i}\right)^2 \frac{1}{V}\sum_j m_j^2 \gamma_j, \tag{3}$$

where m_j is the mass of particle j and $|K_i|^2$ is the dielectric factor of solid ice. It is often more convenient to consider Z as simply being proportional to mass squared in this way (with a correction for non-Rayleigh effects via γ_j) than to use (2) and have to work with the concepts of "diameter" and "density," which can be defined in many different ways for arbitrarily shaped particles. We assume radar attenuation by ice clouds is negligible up to 94 GHz (Hogan and Illingworth 1999).

The parameter we wish to obtain from lidar is visible extinction coefficient, which in the geometric optics approximation is simply twice the sum of particle cross-sectional areas (A) in a unit volume:

$$\alpha = \frac{2}{V}\sum_j A_j. \tag{4}$$

The main problem in the retrieval is that the lidar itself suffers extinction by the cloud for which it must be corrected before combination with radar to estimate particle size. Lidar measures the attenuated lidar backscatter coefficient (β'), which for a near-nadir viewing instrument at height z_0, neglecting the molecular contributions to the extinction and backscatter and assuming single scattering, is given by

$$\beta'(z) = \beta(z)\exp\left[-2\int_z^{z_0}\alpha(z')\, dz'\right], \tag{5}$$

where $\beta(z)$ is the unattenuated backscatter coefficient at height z. If the extinction-to-backscatter ratio $S = \alpha/\beta$ is assumed constant through the profile, then it can be shown that

$$\alpha(z) = \beta'(z)\left[\frac{1}{S} - 2\int_z^{z_0}\beta'(z')\, dz'\right]^{-1}. \tag{6}$$

The problem is that for all but the most optically thin clouds, the retrieved α profile is extremely sensitive to the exact value of S assumed, particularly toward the far end of the cloud. If molecular scattering is detectable beyond the far end of the cloud, then optical depth can be estimated and a stable α profile retrieved (e.g., Klett 1985), but at 355 nm this is possible only for cloud optical depths less than around 2. The threshold is even lower for longer-wavelength lidars. When the molecular signal is not detectable then the α profile cannot be recovered accurately from lidar alone.

The solution adopted by both the KNMI and IPSL algorithms is to use the information available from the radar in the correction procedure; only a very narrow range of S in (6) will produce an α profile that, when combined with the radar, produces a plausible profile of meteorological variables. This approach is a departure from that of Wang and Sassen (2002) and others, who attempt to correct the lidar for extinction independently, before combining with radar.

b. KNMI lidar extinction correction

The KNMI algorithm (Donovan and van Lammeren 2001) hypothesizes that the most likely α profile is that which results in the least fluctuation of retrieved particle size at the far end of the cloud. Rather than using r_e as defined in (1), which involves assumptions on ice particle habit, a "radar–lidar effective radius" r_e' is used:

$$r_e' = \left(\frac{0.93}{|K_i|^2}\frac{\pi}{32}\frac{Z}{\alpha}\right)^{1/4}. \tag{7}$$

The coefficients ensure that in the case of solid Rayleigh-scattering ice spheres of radius r, this expression reduces to

$$r_e' = [\langle r^6\rangle/\langle r^2\rangle]^{1/4}. \tag{8}$$

The definition of an effective radius in terms of the ratio of moments of the size distribution has parallels

with the more familiar definition of effective radius for liquid water clouds as $r_e = \langle r^3 \rangle / \langle r^2 \rangle$ (e.g., Stephens 1978).

A cost function is defined that penalizes gradients in $\ln(r'_e)$ in the farthest few gates of the profile. An iterative procedure then finds the S value in (6) that minimizes this cost function, although note that the algorithm may alternatively be formulated in terms of the total optical depth or the α value at the far end of the profile. Because the natural logarithm of r'_e is taken, the power of (1/4) in (7) has no effect on the retrieval; effectively, we are finding the α profile that minimizes variations in the ratio of Z to α at the far end of the cloud.

c. IPSL lidar extinction correction

The IPSL algorithm (Tinel et al. 2005) is similar to the KNMI algorithm except that it hypothesizes that the best α retrieval results in the least fluctuation of particle number concentration with height. The physical basis behind this is that ice particle growth by vapor deposition and riming results in a change in particle size (and hence r'_e), but not in the number of particles. Rather than attempting to derive the actual number concentration, the concept of a normalized number concentration parameter N_0^* is adopted (Testud et al. 2001; Illingworth and Blackman 2002). For ice clouds it may be defined as

$$N_0^* = \left(\frac{4}{D_m}\right)^4 \frac{\mathrm{IWC}}{\pi \rho_l}, \tag{9}$$

where D_m is the melted-equivalent mass-weighted mean diameter and ρ_l is the density of liquid water. Analysis of aircraft data shows that when moments of the distribution are normalized by N_0^*, precise power-law relationships exist between them. Tinel (2002) derived the following relationship between α (m^{-1}) and Z ($\mathrm{mm}^6\ \mathrm{m}^{-3}$):

$$\frac{\alpha}{N_0^*} = 1.22 \times 10^{-8} \left(\frac{Z}{N_0^*}\right)^{0.415} \tag{10}$$

(where N_0^* is in m^{-4}). This can be rearranged to

$$N_0^* = 3.37 \times 10^{13} \frac{\alpha^{1.71}}{Z^{0.71}}. \tag{11}$$

An iterative procedure then finds the α profile that yields the least variation of N_0^* with range.

So despite appearing to be based on very different principles, the KNMI and IPSL algorithms effectively retrieve the extinction profile in a very similar way: by finding the solution that minimizes variations in the ratio of some power of Z to some power of α. Whether the exact values of these powers are significant will be determined in section 4b.

d. Correction for lidar multiple scattering

The light from spaceborne lidars can undergo more than one scattering event before being returned to the detector, which manifests itself as a range-dependent enhancement of the measured backscatter. The KNMI algorithm accounts for this effect using the multiple-scattering model of Eloranta (1998), coupled with knowledge of the properties of the lidar in question, by replacing (6) with an iterative numerical solution (Donovan and van Lammeren 2001). At the time of this study the IPSL algorithm had no capability to correct for multiple scattering. The significance of this omission is found in blind test 2.

e. Estimation of IWC and effective radius

The last step in the retrieval is to use the combination of Z and α to estimate IWC and r_e. From (1) note that an estimate of one of IWC or r_e implies an estimate of the other. The KNMI algorithm uses the results of Donovan and van Lammeren (2001), who derived relationships between r_e and r'_e by simulating them for idealized monomodal and bimodal distributions of particles with various mass–size relationships taken from the literature. Where not otherwise stated, a single gamma distribution is assumed with the Francis et al. (1998) mass–area relationship, given by

$$\begin{aligned} m &= 691.2A^{1.5}; \quad A \le 5.2 \times 10^{-9}\mathrm{m}^2, \\ m &= 1.275A^{1.17}; \quad A > 5.2 \times 10^{-9}\mathrm{m}^2, \end{aligned} \tag{12}$$

where m is in kilograms and A is in square meters. Donovan and van Lammeren (2001) reported a span of a factor of 2 in retrieved r_e between the various combinations of size distribution and mass–size relationship, although this included hexagonal columns and solid ice spheres that are unlikely to be the dominant habit throughout a cloud profile.

The IPSL algorithm makes use of the N_0^* concept to estimate IWC and r_e. Tinel (2002) used aircraft data to find an empirical relationship between IWC/N_0^* and Z/N_0^*, which is used to infer IWC from observed Z and retrieved N_0^*. For a fixed mass–size relationship there is little scatter between the two, but variations in the relationship in real clouds will feed through to errors in

IWC and r_e in the same way as for the KNMI algorithm (see section 4d).

3. Generation of synthetic radar and lidar profiles

a. Blind test 1: Profiles 1–5

The radar and lidar profiles in the first blind test were simulated from in situ data taken by the Met Office C-130 aircraft during five Lagrangian descents in frontal clouds around the British Isles, 3–6 km thick. The flight patterns consisted of short horizontal runs separated by descents of around 500 m. Ice particle size spectra were measured by the 2D cloud and precipitation probes, spanning the diameter range of 25–6400 μm, and were available binned by both the cross-sectional area A and the mean of the maximum dimensions measured parallel and perpendicular to the photodiode arrays D. The distributions were far from monomodal; the same data were used by Field (2000) to demonstrate the evolution of bimodal size spectra due to aggregation. From each run a single 5-s-averaged size distribution was extracted, corresponding to around 500 m in the horizontal. This is comparable with the horizontal resolution at which spaceborne radar–lidar retrievals would be performed.

The size spectra binned by area were used to calculate the various parameters of interest: α [from (4)], IWC [using (12)], and then r_e [from (1)]. Radar reflectivity at 94 GHz was calculated by approximating the particles as spheres composed of a uniform mixture of ice and air with a diameter equal to the equivalent-area diameter $D_A = 2\,(A/\pi)^{1/2}$. Equation (3) was then applied using the same mass as in the IWC calculation, and using Mie theory to compute γ from D_A.

Five profiles at a vertical resolution of 500 m were generated. The profiles of Z and α were interpolated to 100 m using cubic splines in logarithmic space, thereby simulating the resolution that will be possible from space (oversampled in the case of the radar). Finally, the β' that would be measured by the lidar (in the absence of molecular or multiple scattering) was calculated using (5). For each of the five profiles, two profiles of S were employed—one constant with height and the other varying over around a factor of 2, similar to the range found by Ansmann et al. (1992). The β' values were truncated at 10^{-10} m^{-1} sr^{-1}, which affected profiles 2, 4, and 5. This is much lower than can be measured by any real lidar, but it provides an ultimate test of the extinction-correction capabilities of the algorithms. Figure 1 shows the five Z and ten β' profiles provided to the algorithms. Note that the algorithms had no knowledge of the S values (Fig. 1c) that had been used.

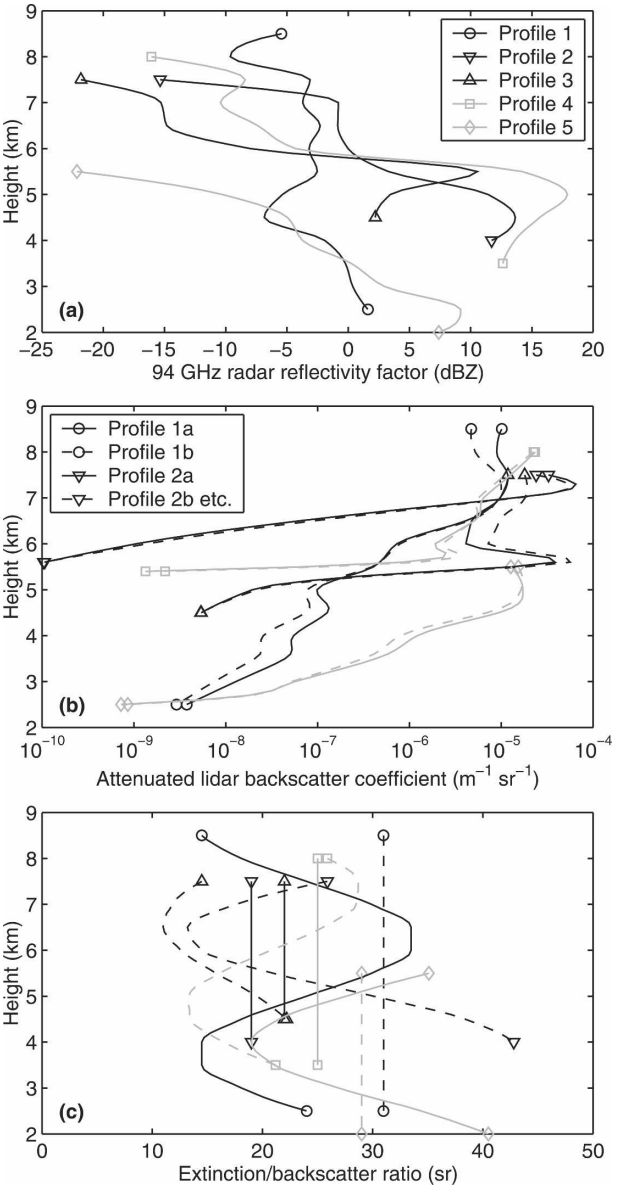

FIG. 1. Profiles used in blind test 1: (a) radar reflectivity factor Z, (b) attenuated lidar backscatter coefficient β', and (c) extinction/backscatter ratio S. The S profiles were not available to the algorithms.

b. Blind test 2: Profiles 6–10

As will be seen in sections 4a and 4d, the first blind test demonstrated the impressive skill of both algorithms, but it omitted a number of instrumental and optical factors that will make retrievals from space more difficult. In blind test 2, these effects were simulated to provide a much more realistic and challenging test. Again, C-130 aircraft size spectra were used, this time from the European Cloud Radiation Experiment (EUCREX). The five new profiles (6–10) were in-

tended to represent a 10-km dwell (1.4 s) from EarthCARE at an altitude of 400 km, following the design specifications of the European Space Agency (2001).

The data were available by D and A. Profiles 7–9 used the mass–area relationship of Francis et al. (1998) as before, but profiles 6 and 10 used the data binned by D for the calculation of both IWC and Z, employing the mass–D relationship of Brown and Francis (1995):

$$\begin{aligned} m &= 480D^3; \qquad D < 9.7 \times 10^{-5}\text{m}, \\ m &= 0.0185D^{1.9}; \quad D \geq 9.7 \times 10^{-5}\text{m}, \end{aligned} \tag{13}$$

where m is in kilograms and D is in meters. The intention was to test the sensitivity of the retrieval algorithms to the mass–size relationship. In practice the KNMI algorithm was run separately for several different mass–size assumptions, which provided a more revealing test of the sensitivity of the algorithm (see section 4d).

The 2D cloud probe is known to be unreliable for measuring particles smaller than 100 μm (Heymsfield and Baumgardner 1985), with the result that the water content in these small particles is underestimated by around a factor of 2.5 (McFarquhar and Heymsfield 1997). We follow Hogan and Illingworth (2003) and correct for this effect by fitting a gamma distribution to the small particle mode. There is considerable uncertainty over the role of small particles, and while this procedure should help to remove the *mean* small-particle IWC bias, it will not accurately reproduce the distribution that occurred in individual cases. However, for the purposes of testing the algorithms it is only important that the size distributions are realistic. The resulting size distributions were frequently bimodal, and the sensitivity of the algorithms to treatment of small particles is addressed in section 4g.

Gaussian smoothing of the Z profile was used to simulate 100-m oversampling of an impulse response function with a two-way half-power full-width of 385 m. Random measurement errors were added following Hogan and Illingworth (1999), assuming 8400 independent samples in 1.4 s and a thermal/instrument background noise of -22.1 dBZ. This yields a minimum detectable signal of -38 dBZ at all altitudes. The more recent specifications given in the European Space Agency (2004) quote a sensitivity of -36 dBZ, although in the cases shown this would have no significant effect on the results. Generally radar errors are small, only ± 0.05 dB at a large signal-to-noise ratio. Gaseous attenuation is not simulated because it is assumed to be characterized well enough that it could easily be corrected in real observations. The resulting profiles are shown in Fig. 2a. Due to its higher orbit, the

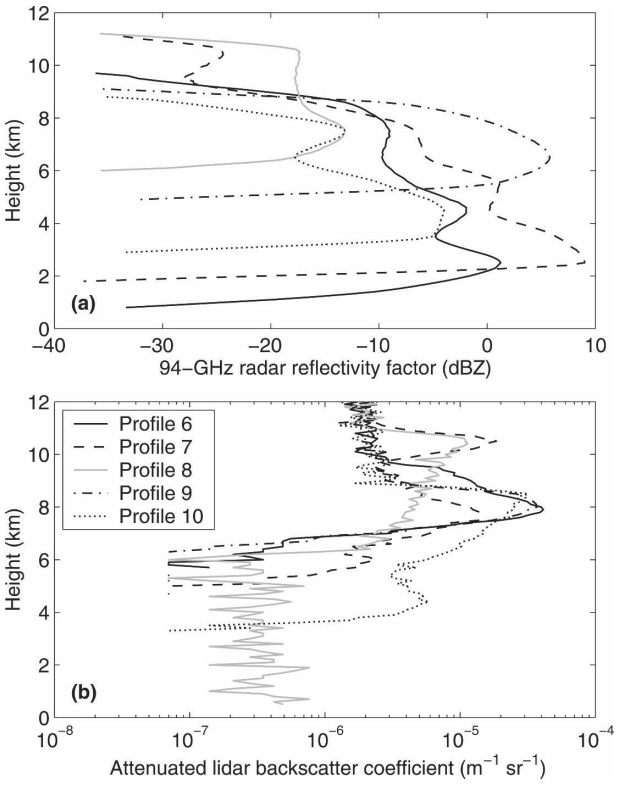

FIG. 2. Profiles used in blind test 2: (a) radar reflectivity factor Z and (b) attenuated lidar backscatter coefficient β'.

CloudSat radar will have a minimum detectable signal of around -28 dBZ at the start of its mission (Stephens et al. 2002), so it would be able to detect the full extent of all of the profiles considered in this study, although perhaps having difficulty with the highest 1 km of profile 7.

The changes to the lidar profile in blind test 2 compared to blind test 1 are much more drastic, as is evident in Fig. 2b. First, the backscatter from the air molecules β_{mol} is added to the unattenuated backscatter profile assuming the following approximate height dependence at 355 nm (Vaughan et al. 1998),

$$\beta_{\text{mol}}(z) = 8.1 \times 10^{-6} \exp(-z/8000), \tag{14}$$

where β_{mol} is in m^{-1} sr^{-1} and height z is in meters. It is assumed that the density profile of the atmosphere is known well enough that this would be possible to calculate accurately in a real retrieval, so it was available to the operators of the algorithms. For the same reason, the extinction due to molecular scattering was not simulated. The molecular return is clearly visible at the top of the profiles in Fig. 2b, and in profile 8 below the cloud as well, albeit a factor of 20 lower due to extinction by the cloud. Operationally, the unattenuated mo-

TABLE 1. Summary of the approximate effect of various factors on the retrieved extinction coefficient (α), effective radius (r_e), IWC, longwave cloud radiative effect, and shortwave cloud radiative effect. Note that radiative effects expressed as a percentage indicate the fractional change in the cloudy minus clear-sky top-of-atmosphere upwelling irradiance.

Source of error	Effect				
	α	r_e	IWC	Longwave	Shortwave
Any error in lidar calibration	No effect	No effect	No effect	No effect	No effect
Radar calibration: reflectivity a factor of 2 too high	No effect	+5 μm	+10%[a]	<2 W m^{-2}	−2%[a]
Any change in absolute value of S	No effect	No effect	No effect	No effect	No effect
S varying by ±25% in a profile	±25%[b]	±2.5 μm[b]	±25%[b]	<2 W m^{-2}	±5%[a]
Uncertainties in the representation of small crystals	No effect	±15%[a]	±15%[a]	<2 W m^{-2}	±3%[a]
Uncertainties in mass–size relationship	No effect	±30%	±30%	<2 W m^{-2}	±6%
Non-Rayleigh radar scattering: true r_e greater than 100 μm	No effect	$\simeq -70$ μm[c]	−40%[a]	<2 W m^{-2}	+10%[a]
Neglecting lidar multiple scattering	−35%[a]	+3 μm[a]	−35%[a]	−15%[a]	−30%[a]
Lidar instrument noise spanning a factor of 2	±35%[b]	±3 μm[b]	±35%[b]	<2 W m^{-2}	<2 W m^{-2}
Difference in radar and lidar footprints	±8%	±1 μm	±8%	<2 W m^{-2}	±2%

[a] Very approximate value.
[b] These errors are fluctuations around the true value, so they may largely cancel when vertically integrated quantities are calculated.
[c] Retrieved effective radius stays constant at around 70 μm (note that this is only a problem for 94-GHz radar).

lecular backscatter would be detected above the highest cloud, and errors of a few percent would be expected in predicting this through the cloudy part of the profile (making additional use of temperature and pressure analyses beneath the satellite). The resulting errors in retrieved cloud optical depth of a few percent are small compared to others described in this paper so may be neglected.

We assume that the other background signals are negligible; that is, the lidar is operating at night and there is no "dark current." In the daytime a background signal would be detected due to scattered solar photons, particularly over dense cloud. However, the worst-case background signal for the EarthCARE lidar would only be around 4×10^{-7} m^{-1} sr^{-1} (European Space Agency 2001, p. 95). From Fig. 2b it can be seen that this would not significantly affect the extent of the cloud detected by the lidar.

Multiple scattering was calculated to fourth order using the Eloranta (1998) formulation, assuming a lidar half-angle beam divergence and a field of view of 0.0258 mrad, which yields a footprint of 20 m at the height of the cloud. The accuracy of the Eloranta model is evaluated in the appendix by comparison with a Monte Carlo simulation.

The sensitivity of the retrievals to variations in S with height was examined fully in blind test 1, so here S was kept constant with height, although a different value (unknown to the algorithms) was used in each profile.

The final step is to add lidar instrument noise, which we calculated assuming the lidar receiver to be a photon counter. For the resolution considered here (10 km horizontally and 100 m vertically), a single photon detected by the EarthCARE lidar would correspond to a backscatter coefficient of 7×10^{-8} m^{-1} sr^{-1}. Fluctuations have been applied based on Poisson statistics, such that the reported values of β' are quantized into multiples of 7×10^{-8} m^{-1} sr^{-1}. The resulting error is proportional to the square root of the mean, and hence the *relative* error decreases at higher signal levels, an effect apparent in Fig. 2b.

4. Results

We examine each of the various sources of error in turn and present selected profiles that demonstrate the effect on the retrievals. The findings of this section and the next are summarized in Table 1.

a. *Sensitivity to the lidar extinction-to-backscatter ratio*

Figure 3 shows true α for the profiles of blind test 1 and the corresponding values retrieved by the IPSL algorithm. For each profile there are two retrievals corresponding to the different S profiles used (shown in Fig. 1c). Note that the retrievals in the case of S constant with height (dashed lines) are remarkably good, in most cases lying directly beneath the true curves. For S varying with height (dotted lines), the lidar inversion is still perfectly stable, but where the local S value is higher than the mean value in the profile by a certain factor then α is underestimated by the same factor, and conversely when the local S value is lower.

For both the constant and variable S profiles, the α retrievals of the KNMI algorithm (not shown) are almost identical to those of the IPSL. The only difference lies in the lowest few hundred meters of each profile

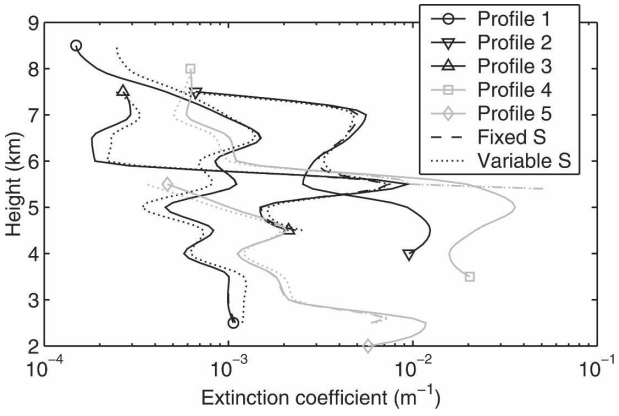

FIG. 3. Visible extinction coefficient from blind test 1: true values (solid lines), IPSL retrieval in the case of constant S with height (dashed lines), and IPSL retrieval for variable S with height (dotted lines). Note that some of the dashed lines lie directly beneath the solid lines.

where they begin to diverge from each other and from the true extinction. The implications of this are examined in the next section.

We next consider the effect of S on the retrievals of IWC and r_e. It is clear from (1) that any error in the retrieved α will feed through to one or both of these parameters. Figure 4 shows a comparison of the true values with those from the KNMI algorithm for profiles 1 and 4. Profile 1 shows differences due to non-Rayleigh radar scattering that will be discussed in section 4c, so we consider profile 4, which is representative of the other three profiles of blind test 1. The gray dashed and dot–dashed lines show the retrievals in the case of constant S and that varying with height, respectively (note that the algorithm has assumed the same mass–size relationship as was used in generating the profiles). Between 6 and 7 km, the retrieval with constant S underestimates r_e by around 4 μm, but the difference between the constant and variable S retrievals is only 1 μm (i.e., 2%). Figure 3 shows that the corresponding difference in α at this location was 20%. This demonstrates the point made previously that retrieved particle size should be very insensitive to errors in either Z or α. As seen in Fig. 4a this 20% underestimate in α corresponds to an underestimate in IWC by the same amount.

It should be noted that when considering vertically integrated quantities such as optical depth and ice water path, there would be some degree of cancellation in the errors at various heights caused by variable S; an overestimate of α or IWC at one height will partially offset an underestimate of these parameters at another height.

The problem of variable S would be much more severe for lidars viewing within 1° of nadir, because of specular reflection from horizontally aligned plate crystals (Thomas et al. 1990). This could result in a dramatic reduction in S in layers where plates can predominate, such as between −9° and −23°C. Spaceborne lidar should therefore be pointed a few degrees from nadir.

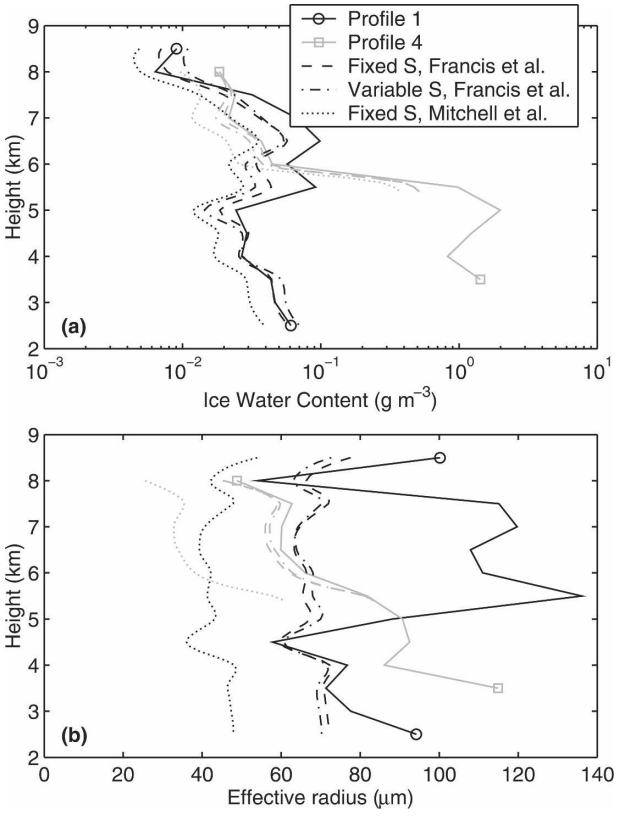

FIG. 4. Ice water content and effective radius from profiles 1 and 4 of blind test 1: true values (solid lines), KNMI retrieval assuming the same Francis et al. (1998) mass–size relationship that was used in generating the profiles (dashed lines), and KNMI retrieval assuming the different Mitchell et al. (1996b) mass–size relationship (dotted lines).

b. Sensitivity to lidar extinction correction technique

Blind test 1 should be regarded as a very stringent test of the algorithms; by providing them with β' down to 10^{-10} m^{-1} sr^{-1}, their ability to correct for one-way optical depths of up to 7 (i.e., signals depleted by a factor of 10^6) has been evaluated. The results reported in the last section are very encouraging, with both algorithms able to recover α accurately through most of the profile. If S varies within a profile and no other a priori information is available on the nature of the cloud, then the biases evident in Fig. 3 are probably unavoidable.

Table 2 shows the true optical depth of each of the

TABLE 2. True and retrieved optical depths for blind test 1 (profiles 1–5) and blind test 2 (profiles 5–6) for constant S with height. The optical depths of the full profile are shown in column 2, but note that only in profiles 1, 3, and 8 did the lidar detect the full extent of the cloud. Column 3 shows the optical depth from cloud top down to the depth of lidar penetration, and columns 4 and 5 show the associated errors in the KNMI and IPSL retrievals. Because most of the retrieval error occurs in the lowest 400 m, column 6 shows the optical depth down to 400 m above the lidar penetration depth, with the errors in the retrievals down to this depth in columns 7 and 8. Note that the large errors in the IPSL retrievals in profiles 6–10 are due to its neglect of multiple scattering in blind test 2 (see section 4e).

		Optical depth to lidar penetration			Optical depth to lidar penetration −400 m		
Profile	Full optical depth	True	KNMI error	IPSL error	True	KNMI error	IPSL error
1	4.739	4.739	+0.120	+0.002	4.326	+0.041	−0.006
2	21.670	7.157	−0.057	+0.216	6.092	−0.342	−0.331
3	5.002	5.002	−0.888	−0.392	4.300	−0.588	−0.434
4	52.908	8.331	−2.885	+1.205	2.060	−0.012	−0.013
5	11.830	7.231	−0.706	−1.009	3.992	−0.040	−0.042
Mean absolute error (profiles 1–5)			0.93 (14%)	0.56 (9%)		0.20 (5%)	0.17 (4%)
6	13.858	3.640	+1.437	−1.174	2.881	+0.039	−1.018
7	22.267	3.525	+0.803	−1.117	2.693	+0.230	−0.824
8	1.421	1.421	+0.209	−0.660	1.407	+0.195	−0.646
9	8.016	4.031	+0.471	−1.315	2.679	+0.067	−0.861
10	5.724	5.688	−2.166	−2.709	4.226	−0.891	−1.504
Mean absolute error (profiles 6–10)			1.02 (28%)	1.74 (48%)		0.28 (10%)	0.97 (35%)

profiles and the associated errors in the retrieved values in the case of S being constant with height. Of course, where the lidar loses signal in the middle of the cloud it is impossible to estimate the full optical depth, so columns 4 and 5 show the errors in the estimate of optical depth down to the depth of the lowest measurable lidar return. Considering the five profiles of blind test 1, the mean absolute error in retrieved optical depth is 0.93 (14%) for the KNMI algorithm and 0.56 (9%) for the IPSL algorithm, which is seemingly higher than the errors indicated by the dashed lines in Fig. 3. However, most of this error occurs in the lowest 400 m of the cloud (or the last 400 m that the lidar has a signal), where the assumption of constant r_e' or N_0^* has the most effect on the retrieval. The last two columns of Table 2 show that when the lowest 400 m of the profile is excluded from the calculation of optical depth, the error is considerably less (around 0.2, or 5%) in blind test 1. The KNMI errors in blind test 2 are around twice as large, possibly due to difficulties with the boundary assumptions when multiple scattering degrades the lidar signal. The large IPSL errors in blind test 2 are due to uncorrected multiple scattering, discussed in section 4e. In section 5 the sensitivity of the radiative fluxes to these various errors is evaluated.

These differences in optical depth suggest that refinements could be made to the extinction-correction procedure. The lower mean error in the IPSL retrievals in blind test 1 suggests that it may be more realistic to consider N_0^* constant at the far end of the cloud than r_e'. However, the aircraft data used here do not represent true vertical profiles, so the behavior of r_e' and N_0^* at cloud base is not necessarily realistic. A combined approach would be to use a cost function that penalizes gradients in both N_0^* and r_e', and possibly also in α. Either more aircraft data or actual ground-based radar–lidar retrievals would have to be studied to determine the best form of such a cost function.

c. Sensitivity to non-Rayleigh radar scattering

The retrieval of particle size is possible because Z is a much higher moment of the size distribution than is α. However, at high radar frequencies such as 94 GHz, a problem occurs when large non-Rayleigh scattering particles are present [i.e., $\gamma < 1$ in Eq. (3)]. While this can be taken into account to some degree by the retrieval algorithm, it was shown by Hogan et al. (2003) that for $r_e > 90$ μm, and assuming the Francis et al. (1998) mass–area relationship, the non-Rayleigh scattering effectively renders Z a *lower* moment of the distribution than α, and the capability to infer size is lost.

The problem is demonstrated in Fig. 4. While profile 4 shows excellent agreement between truth (solid line) and retrieval (dashed line), in both IWC and r_e, the retrieval in profile 1 predicts r_e values of around 70 μm when the true values are closer to 140 μm. Because α is still retrieved very accurately, it is clear from (1) that IWC must also be underestimated by around a factor of 2, and this is indeed what is found. This problem seems unavoidable at 94 GHz, and while a solution from the ground is to use a lower frequency, such as 35 GHz, requirements on sensitivity, beamwidth, and power consumption mean that this solution is unlikely to be considered from space.

d. Sensitivity to the mass–size relationship

The mass–size relationship of Francis et al. (1998) was used to generate all of the profiles in blind test 1 and was also used in the IPSL retrievals. The KNMI algorithm was run twice for each profile—once assuming the Francis et al. relationship and once assuming the "planar polycrystal" relationship of Mitchell et al. (1996b):

$$\begin{aligned} m &= 818.1A^{1.54}; \quad A \le 3.97 \times 10^{-9}\text{m}^2, \\ m &= 8.236A^{1.303}; \quad A > 3.97 \times 10^{-9}\text{m}^2, \end{aligned} \tag{15}$$

where m is in kilograms and A is in square meters. This thereby enabled the effect of changes in the mass–size relationship to be tested. The first thing to note is that the retrieval of α is independent of assumptions on the size distribution or the mass–size relationship. As discussed in section 3c, both algorithms retrieve α by minimizing the variation with height of the ratio of some power of Z to some power of α, and the near-identical results from the two algorithms indicate that the actual powers used are not important through most of the depth of the cloud.

The dotted lines in Fig. 4 demonstrate the effect on IWC and r_e of assuming a different mass–size relationship in the retrieval to that of the "real" cloud. In these cases both are underestimated by 30%. The reason is that up to a maximum dimension of 2 mm, the planar polycrystals of Mitchell et al. (1996b) have a lower mass for a given size than is predicted by the relationship of Francis et al. (1998). The difference increases toward smaller sizes, with the Francis et al. (1998) relationship representing particles smaller than 100 μm as solid ice, while the Mitchell et al. (1996b) relationship has these particles with a density around half that of solid ice. This results in lower r_e for a given r_e' (see Fig. 10 of Donovan and van Lammeren 2001). Note that other radar-based algorithms are also sensitive to this uncertainty, as are passive satellite retrievals (e.g., Baran et al. 1999). The significance of errors in IWC and r_e of this magnitude for radiative fluxes is explored in section 5b.

e. Sensitivity to lidar multiple scattering

The effect of multiple scattering, molecular scattering, and instrument noise on the direct lidar measurements is demonstrated in Fig. 5, which shows two blind test 2 profiles together with the profiles that would have been observed in the absence of these effects (i.e., using the blind test 1 method). The effect of multiple scattering is clearly apparent as an enhancement of the backscatter that increases with range as the lidar beam penetrates further into the cloud, reaching in excess of a factor of 5 at the location of the lowest lidar echo.

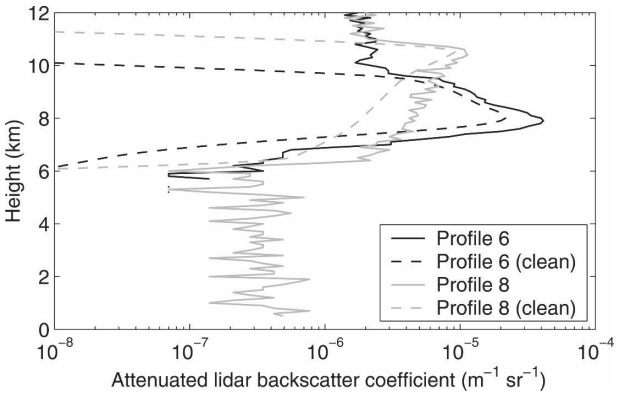

FIG. 5. Attenuated backscatter coefficient from profiles 6 and 8 of blind test 2 (solid lines) together with the "clean" profiles that would have been observed in the absence of multiple scattering, molecular scattering, and instrument noise (dashed lines).

Figure 6 shows the true α profiles for these two cases, together with the retrievals by the two algorithms. The KNMI algorithm performs very well, demonstrating that it is possible to account for the strong effect of multiple scattering. It should be noted that the test is somewhat unrealistic because the Eloranta (1998) multiple scattering approximation was used in both the simulation and the retrieval, although it is shown in the appendix that for the viewing geometry of the EarthCARE lidar (in particular the small footprint), the Eloranta formulation compares very closely to a full Monte Carlo simulation.

The effect of neglecting multiple scattering in the

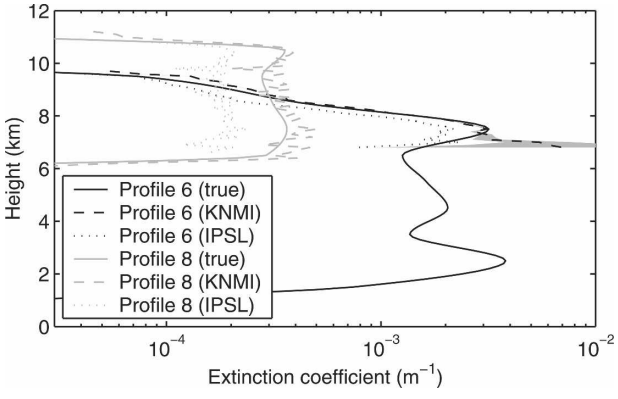

FIG. 6. Visible extinction coefficient for profiles 6 and 8 of blind test 2: true values (solid lines), KNMI retrievals accounting for the effect of multiple scattering (dashed lines), and IPSL retrievals neglecting the effect of multiple scattering (dotted lines). The gray shading indicates the expected error in the KNMI retrieval for profile 6 corresponding to a fractional error of 0.5 at the farthest lidar gate.

retrieval is shown by the IPSL profiles in Fig. 6, which underestimate α by between 30% and 40%. In Table 2 note that the underestimate in total cloud optical depth is also of this order. It might seem counterintuitive that when β' is higher than in the case of no multiple scattering, the algorithm produces an extinction that is too low. The crucial point here is that it is the *gradient* in β' that is used by the algorithm, not the absolute value itself. Figure 5 shows that multiple scattering has the effect of making β' decrease less rapidly with range, which the retrieval algorithm interprets as being due to weaker extinction. This underestimate of α constitutes the largest error in Table 1, highlighting that it is essential for multiple scattering to be accounted for in any algorithm. Multiple scattering has recently been incorporated into the IPSL algorithm.

Figure 6 shows that in the lowest 400 m of profile 6 the KNMI retrieval diverges significantly from the true profile, with an overestimate in α of up to a factor of 5. This effect was discussed for the blind test 1 results in section 4b; but with the realistic instrument sensitivities included in blind test 2, we are now able to estimate the errors that would be expected due to an error in the boundary value assumption. If the fractional error in r_e' (equivalent to the rms error in $\ln r_e'$) at the farthest detectable lidar gate is assumed to be 0.5, then from (7) the fractional error in α will be 2. From (6) the fractional error in S is computed, and hence the error in α at each gate. The result is shown by the gray shading in Fig. 6 and indeed significant error is only expected for the lowest 400 m of the retrieval.

f. Sensitivity to instrument noise and molecular scattering

The lidar instrument noise in Fig. 5 appears as fluctuations in retrieved α in Fig. 6, but crucially has not affected the stability of the inversion. The corresponding r_e profiles are shown in Fig. 7. The systematic differences are discussed in the next section, but here the important thing to note is the much lower fluctuation of retrieved r_e than α, due to the insensitivity of retrieved size to errors in α discussed earlier (the dependence of the ratio Z/α on the fourth power of size implies that the fractional error in α will be 4 times larger that in r_e). Therefore, by (1), fluctuations tend to be present in IWC of a similar magnitude to those in α.

Instrument noise also effectively sets a limit on the sensitivity of the lidar, and thus to the depth into the cloud to which the algorithm can be applied. It should be noted that the fluctuations simulated are specific to a photon-counting detector.

As is evident in Fig. 2, radar instrument noise is negligible compared to lidar noise, and its specific effect cannot be detected by eye in the retrievals. Molecular scattering does not seem to have had any detectable effect on the retrievals, despite neither algorithm having taken account of its contribution to backscatter. Note that techniques exist to distinguish objectively the lidar molecular and ice cloud returns (e.g., Morille et al. 2005, manuscript submitted to *J. Atmos. Oceanic Technol.*), and depolarization can also be used.

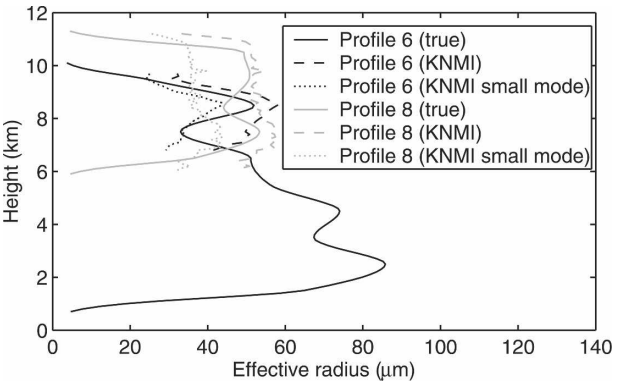

FIG. 7. Effective radius for profiles 6 and 8 of blind test 2: true values (solid lines), standard KNMI retrieval (dashed lines), and KNMI retrieval assuming the presence of a small crystal mode in the size distribution (dotted lines).

g. Sensitivity to the shape of the size distribution

As with the mass–size relationship, the shape of the size distribution has no effect on the retrieval of extinction, so we concentrate on IWC and r_e. Profile 4 in Fig. 4 seems to indicate that in the absence of other sources of error (such as variable S or a different mass–size relationship being used in simulation and retrieval), IWC and r_e can be retrieved to within 5%; similar accuracies were seen for profiles 2, 3, and 5 of blind test 1 (profile 1 being adversely affected by non-Rayleigh radar scattering). This can be regarded as the residual error resulting from uncertainties in the size distribution. It is surprisingly low given that the spectra used in blind test 1 are distinctly bimodal. However, it was only in blind test 2 that a correction was made to counter the problem of undercounting small crystals by the 2D cloud probe.

Figure 7 shows r_e from profiles 6 and 8 of blind test 2. Two KNMI retrievals are shown for each case—one assuming that the size distribution may be represented by a single gamma distribution, and the other assuming the presence of an additional small ice crystal mode in the distribution following Mitchell et al. (1996a). Without the small crystal mode, the retrieval overestimates r_e by, on average, 15%, and with the correction r_e tends to be underestimated by the same amount. We surmise

that the small mode added in the KNMI algorithm is twice as large as the gamma distribution fitted to the EUCREX size spectra to generate the profiles of blind test 2 (see section 3b). The variability in the small mode in the size spectra of ice clouds is an area of active research, but it would seem from this study that there is an error of around ±15% in both retrieved r_e and IWC, resulting from uncertainties in the nature of the size distribution.

h. Sensitivity to instrument calibration

While errors in instrument calibration were not simulated in the blind tests, from the equations involved and what has been learned so far, we can determine the effect they would have. In the case of the radar, a calibration offset would not affect the extinction correction described in sections 2b and 2c, because only the fractional variation of Z with range is considered. The retrieval of IWC and r_e would be affected, however. If the Francis et al. (1998) mass–area relationship is assumed, then Fig. 12 of Hogan et al. (2003) shows that for r_e between 20 and 80 μm, a factor-of-2 increase in the ratio Z/α (e.g., due to a 3-dB error in Z) corresponds to a change in r_e of only 5 μm. The combination of surface returns from the ocean and a comparison with independently calibrated airborne radars should allow calibration of the radar to 1.5 dB (Stephens et al. 2002).

Lidar calibration has no effect on any of the retrieved parameters, because only relative changes in β' are used in the retrieval; the absolute value is not important. This fact is illustrated by noting that changing the lidar calibration would have the same effect as multiplying S by a constant factor through the whole profile, and it has already been shown that the retrieval of extinction is completely insensitive to the absolute value of S. The lidar is relatively easy to calibrate from space using the molecular return.

i. Effect of the difference in radar and lidar footprints

A full-width half-power footprint of 700 m is proposed for the EarthCARE radar, while the lidar footprint will be only around 20 m. Each 0.1-s radar average will be compared to 10 shots from the 100-Hz lidar, sampled across the middle of the radar footprint. Both would use a 500-m vertical average in combined retrievals. The difference in the volume of cloud sampled will have an impact on the retrievals due to cloud inhomogeneity. It was estimated by the European Space Agency (2001) that the rms difference in mean radar reflectivity or mean lidar backscatter, when averaged over these two different sample volumes, would be less than 8% for a typical cirrus cloud. We therefore take this as the estimated error in retrieved α and IWC in Table 1. The effect is equivalent to a variation of S in the profile, so we are able to scale the results for errors in r_e and the shortwave cloud radiative effect.

Errors in instrument alignment would have potentially more serious consequences; the European Space Agency (2001) estimated a 70% error for a footprint separation of 3 km. For CloudSat and Calipso this separation would occur for a pointing error of only 0.25° between the two satellites.

5. Radiation calculations

a. Introduction

This section describes the results of radiation calculations performed on the true and retrieved profiles, which we use to assess the radiative implications of the sensitivities found in section 4. For brevity, only one representative profile is shown from each of the blind tests, but this is sufficient to illustrate the effect of all of the various factors.

The 1D Edwards and Slingo (1996) radiation code is used, assuming a solar zenith angle of 60° and a surface albedo of 0.2, with no low cloud present. Thus, the top-of-atmosphere (TOA) downwelling solar irradiance is 685 W m^{-2} in each profile. The clouds are assumed to be horizontally homogeneous and are embedded in the McClatchey et al. (1972) standard midlatitude summer atmosphere. Relative humidity was set to 100% with respect to ice within the cloud. The shortwave calculations employed 24 spectral bands while the longwave calculations used 9 spectral bands, and ice particle properties were parameterized following Slingo and Schrecker (1982). In reality, 3D radiative effects may be important, but inclusion of these is beyond the scope of this paper.

b. Example from blind test 1: Profile 3

The first case considered is the KNMI retrieval of profile 3 of blind test 1, in which the full extent of the cloud was detected by the lidar. We first consider the "best case," that is, constant S and the same mass–size relationship used in the simulation and the retrieval. This is shown by the dashed lines in Fig. 8. In the longwave the agreement is striking, with a difference of only around 2 W m^{-2} in outgoing longwave radiation (OLR), and little more at any point in the profile. In the shortwave, however, the upwelling TOA irradiance is underestimated by 35 W m^{-2} (or 20% when expressed as a fraction of the cloudy minus clear-sky upwelling fluxes), with the difference originating between 5 and 6

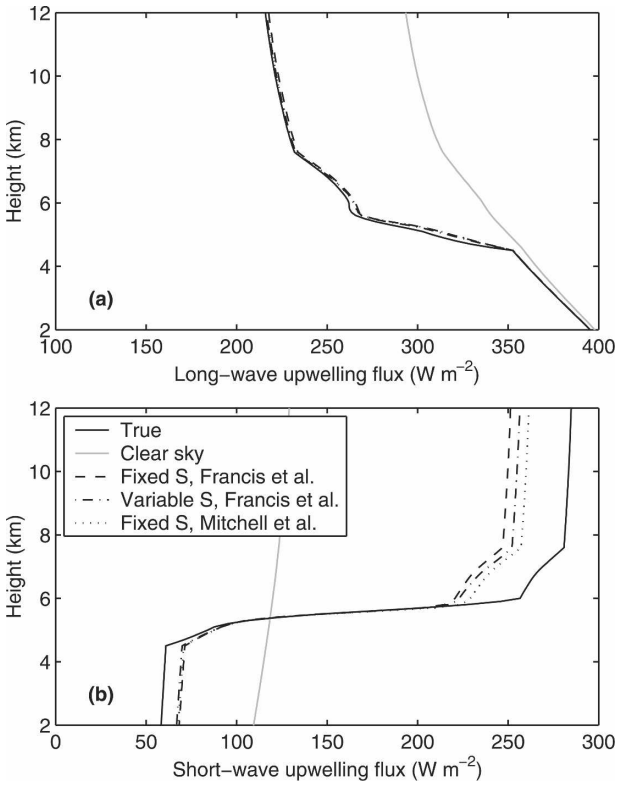

FIG. 8. Upwelling fluxes from profile 3 of blind test 1, calculated both for the true profile and three different KNMI retrievals.

km. Table 2 shows that the KNMI algorithm underestimated optical depth by 0.9 (20%), and likewise in Fig. 3 we see for the IPSL algorithm that the magnitude of the strong spike in α at 5.5 km is underestimated by around 20%. Because this is the most optically thick part of the cloud, it is the region that is most sensitive to errors. This initial test has clearly demonstrated the large difference between the behavior of the shortwave and longwave fluxes: in the shortwave the reflected flux is sensitive to the total optical depth of the cloud, while in the longwave the dependence quickly saturates, and the cloud behaves as a blackbody. Note that errors in downwelling surface shortwave radiation are typically of the same magnitude as the errors in the upwelling TOA shortwave. Additionally, because the relationship between optical depth and shortwave cloud albedo has not saturated for the modest optical depths considered here, we may easily estimate the errors in shortwave fluxes for the other profiles from the errors in optical depth listed in Table 2.

We next consider the effect of a variable S profile. In Fig. 3 it can be seen that in profile 3, variable S led to an overestimate of α by around 25% in the topmost 1.5 km of the cloud, although the total optical depth was still underestimated by 0.620 (as opposed to 0.888 for the constant S profile). The effect on the radiation is consequently quite small: a decrease of 1 W m^{-2} in the longwave and an increase of 6 W m^{-2} in the shortwave. Expressed relative to the clear-sky upwelling irradiance, the values become 2% and 5%, respectively. In the longwave the cloud is still acting very much as a blackbody, while in the shortwave the total optical depth is important, with the vertical location of the most optically thick parts of the cloud being virtually irrelevant.

Figure 8 also shows the fluxes corresponding to the Mitchell et al. (1996b) polycrystal assumption being used in the KNMI algorithm. As in all the profiles of blind test 1, this assumption results in a 30% reduction in the retrievals of both r_e and IWC, although of course α is unaffected. However, it is interesting that it appears to have only a 5% effect in the shortwave and a negligible effect in the longwave. This highlights the critical point that α is the most important parameter in determining the radiative fluxes in both the longwave and shortwave. Effective radius [and from Eq. (1), IWC] determines the single scatter albedo and asymmetry factor of the particles, but these play a less significant role. It is therefore fortunate that α is what is retrieved with most accuracy by the combined radar and lidar.

c. *Example from blind test 2: Profile 6*

Figure 9 depicts the upwelling fluxes for profile 6 of blind test 2. The full extent of this profile was not detected by the lidar so no retrieval was possible in the lower part of the cloud. In an operational algorithm from space one would retrieve the full profile by reverting to a radar-only retrieval in the lower part, but nonetheless this case illustrates several important points. First, the OLR predicted by the KNMI algorithm is accurate to better than 1 W m^{-2} despite only the top 1 km or so being retrieved. This highlights again the fact that OLR is only really sensitive to α near cloud top, and the depth of penetration of a lidar with realistic sensitivity is more than adequate to characterize enough of the cloud. By contrast, the shortwave upwelling TOA irradiance is underpredicted by 80 W m^{-2}, because in the shortwave the full optical depth is important.

The impact of neglecting multiple scattering, which resulted in extinction being underestimated (see Fig. 6), is shown by the comparison of the KNMI and IPSL fluxes. The longwave effect of the cloud retrieved by the IPSL algorithm is 13% less than that of the cloud retrieved by the KNMI algorithm at TOA, although this underestimate varies between 5% and 30% for the five profiles of blind test 2. The underestimate in the shortwave is greater, varying between 15% and 40%.

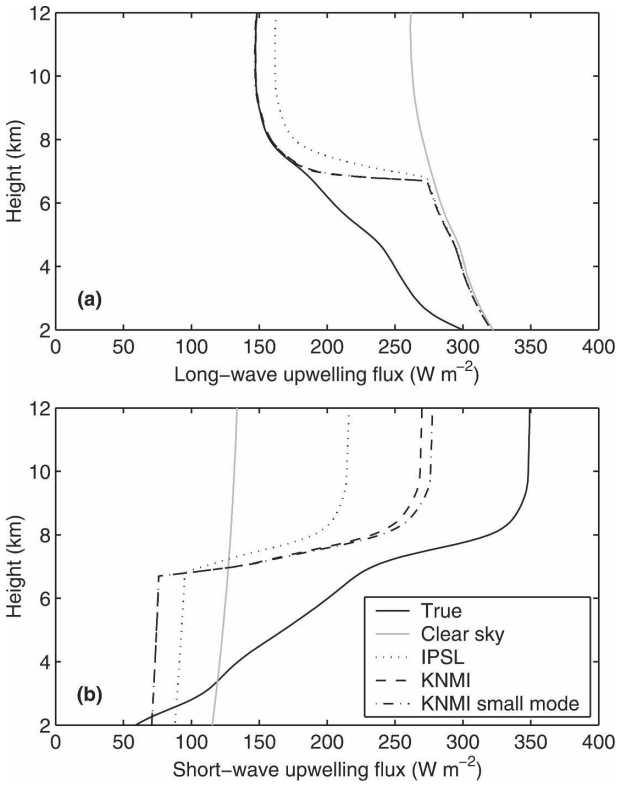

FIG. 9. Upwelling fluxes from profile 6 of blind test 2 calculated for the true profile, the IPSL retrieval, and the KNMI retrievals both with and without the inclusion of a small-particle mode in the distribution.

Representative mean values of this bias are given in Table 1.

Next, the effect of assumed size distribution is examined. As seen in Fig. 7 the inclusion of a "small mode" in the KNMI algorithm results in a 30% reduction in predicted r_e (and IWC). In Fig. 9b it can be seen that this results in only a 7% increase in the effect of the cloud in the shortwave, which is close to the 5% found for the same change in r_e in section 5b. So, for this configuration of the radiation code we can say that for a fixed extinction profile, the fractional change in the effect of a retrieved cloud on the shortwave fluxes would be around 20% of any fractional change in r_e. By contrast, for the modest optical depths considered here there is an approximately linear relationship between shortwave cloud albedo and optical depth for constant r_e.

In profile 6 of Fig. 6 it was seen that just before the lidar lost signal at around 7 km, the KNMI retrieval produced an erroneous "spike" in α. The retrieval error expected in the lowest few hundred meters was high, but it is nonetheless worthwhile commenting on the effect on the radiation field. In Fig. 9, both the long-wave and shortwave fluxes show a very sharp gradient at 7 km, which when the downwelling fluxes are also considered, corresponds to a heating rate of 60 K day^{-1}. This is unrealistically high for ice clouds and highlights the need for algorithms to ensure stability at all locations. One solution (also discussed in section 4b) would be to add a term to the cost function used in section 2b to penalize sharp changes in α, as well as in r_e' or N_0^*.

More generally there is a need to investigate how best to extend the retrieval through the full depth of the cloud after the lidar has lost signal, although implementation of such a scheme is beyond the scope of this paper. Switching to empirical relationships based on Z alone would result in a sudden jump in the derived parameters, so a better approach would be to make use of the information gained where the lidar still has a signal to retrieve more accurate (and smoother) profiles beneath, perhaps in the framework of optimal estimation theory.

6. Discussion and conclusions

In this paper the ability of spaceborne radar and lidar to retrieve the important microphysical parameters of ice clouds has been tested, with specific examination of the sensitivities to numerous sources of error, as summarized in Table 1. The results are applicable to both EarthCARE (European Space Agency 2004) and the CloudSat/Calipso satellites (Stephens et al. 2002). The main strength of the technique is the accuracy of the retrieved extinction profile (optical depth to 400 m above the lowest lidar return retrieved with an error of ± 0.2) and its insensitivity to assumptions on the nature of the size distribution, the habit of the particles, or errors in instrument calibration. Extinction retrievals using the molecular return at the far side of the cloud (Klett 1985) or high spectral resolution lidar (European Space Agency 2004) are limited to much less optically thick clouds than those of the radar–lidar method.

Retrievals of IWC and r_e are sensitive to the assumed ice particle mass–size relationship (errors of up to $\pm 30\%$ expected) and, to a lesser extent, the presence of small ice crystals, although these factors play a much less significant role in determining radiative fluxes than α. It should be pointed out that these problems are common to other radar algorithms (e.g., Hogan et al. 2000; Matrosov et al. 2002), but without the accurate retrieval of α available from the inclusion of lidar information, inferred radiative fluxes would be expected to be much less accurate.

We have demonstrated the need to account for lidar multiple scattering in the retrieval; for EarthCARE the

neglect of this effect results in optical depth being underestimated by around 35%. For narrow beamwidth lidars, the Eloranta (1998) multiple scattering formulation agrees well with the much more computationally expensive Monte Carlo simulations, so it may be used with confidence in retrieval algorithms.

Longwave fluxes calculated from the derived profiles are found to be remarkably accurate compared to the "true" profiles, with errors of around 2 W m^{-2} near the cloud top, and of this order throughout the profile if the lidar is able to fully penetrate the cloud. Shortwave errors are larger, being directly related to errors in retrieved optical depth. Of the three profiles penetrated fully by the lidar (profiles 1, 3, and 8) the mean absolute error in retrieved optical depth from the KNMI algorithm was 12%, leading to around the same error in shortwave fluxes compared to those of clear sky. Further work is required to investigate how best to combine the radar–lidar approach with other techniques and measurements to retrieve a best estimate of the full profile when the lidar does not penetrate the cloud.

The success of using "blind tests" based around aircraft-simulated profiles suggest that this approach would be well suited to testing other retrieval algorithms, particularly combinations of active and passive sensors.

Acknowledgments. We are grateful to Paul Field and Phil Brown at the Met Office for providing the aircraft data used in the two blind tests. This research was funded by the European Space Agency Grant 15741/01/NL/SF.

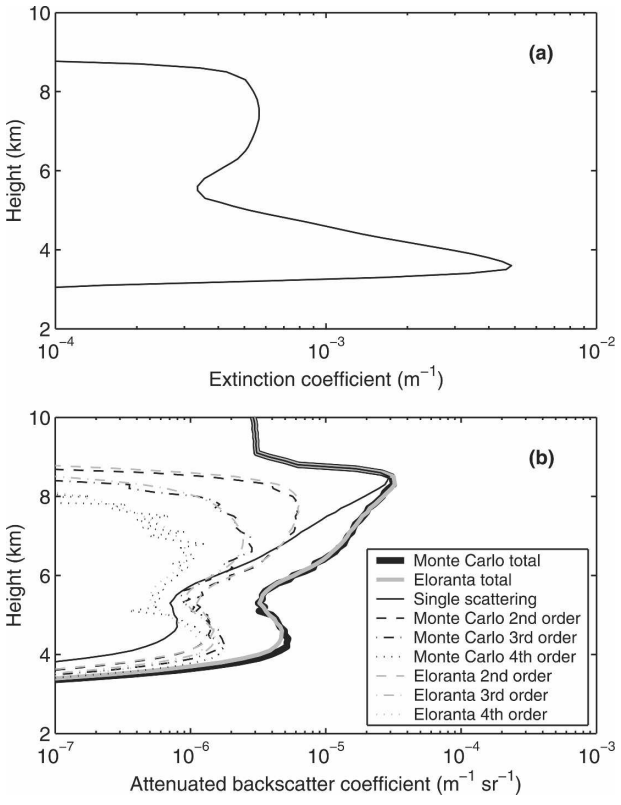

FIG. A1. (a) Extinction coefficient for profile 10 of blind test 2, and (b) comparison of the corresponding backscatter profiles predicted by a Monte Carlo simulation and the Eloranta (1998) formulation (thick lines), together with the individual scattering components up to fourth order (thin lines). Note that the single scattering (first order) contribution is easily calculated and is the same for both methods.

APPENDIX

Comparison of Multiple Scattering Simulations Using Monte Carlo and Eloranta Codes

In this appendix we compare the performance of the Eloranta (1998) multiple scattering model (used by both the KNMI algorithm and in the simulated profiles of blind test 2) with a Monte Carlo simulation for the geometry of the EarthCARE lidar described in section 3b and the European Space Agency (2004). The Monte Carlo simulation utilized phase functions that are appropriate for slightly roughened hexagonal plates (Hess et al. 1998), which have similar S values to those in section 3. It analytically calculates the unscattered energy from the lidar at each altitude and then computes the higher-order scattering by launching a number of appropriately weighted photon packets from each altitude bin (typically 2000–5000 photons per altitude bin). As the photon packets propagate and scatter, for each scattering event, the signal received by the lidar is calculated analytically. To increase the efficiency of the calculation, the technique of forcing scattering of the photon packets to occur within a specified distance from the receiver axis was implemented (Platt 1981). Both the Eloranta and Monte Carlo calculations were performed to fourth order.

Figure A1a shows the extinction coefficient for profile 10 of blind test 2. The effective radius (not shown) ranged between 40 and 120 μm through the bulk of this profile. Figure A1b shows a comparison between the two simulated backscatter profiles for this case, and for clarity the effects of instrument noise have not been included (as they were in Fig. 2). The Eloranta model agrees very well with the Monte Carlo prediction, with an rms difference of only 4% between 4.5 and 8.5 km. This is despite the fact that multiple scattering has increased the apparent backscatter over the single scattering value by a factor of 6 in the lower part of the

cloud. The individual scattering components also agree well, and most of the difference in the total is likely to be statistical noise in the higher-order components of the Monte Carlo simulation. The slight underestimate by the Eloranta model beneath 4.5 km is believed to be due to it approximating the forward-scattering lobe of the phase function by a single Gaussian. There is evidence that scattering beyond the fourth order may be important below 4.5 km, but this could also be represented by the Eloranta model. Similar results (not shown) have been obtained for the other blind test cases.

We conclude that the Eloranta (1998) model is sufficiently accurate for use in both retrieval algorithms and the blind test simulations in this paper. However, this result is specific to the small (20 m) footprint of the EarthCARE lidar, and Monte Carlo comparisons would need to be repeated if the Eloranta model was to be used for larger-footprint lidars.

REFERENCES

Ansmann, A., U. Wandinger, M. Riebesell, C. Weitkamp, and W. Michaelis, 1992: Independent measurement of extinction and backscatter profiles in cirrus clouds by using a combined Raman elastic-backscatter lidar. *Appl. Opt.,* **33,** 7113–7131.

Baran, A. J., P. D. Watts, and P. N. Francis, 1999: Testing the coherence of cirrus microphysical and bulk properties retrieved from dual-viewing multispectral satellite radiance measurements. *J. Geophys. Res.,* **104,** 31 673–31 683.

Brown, P. R. A., and P. N. Francis, 1995: Improved measurements of the ice water content in cirrus using a total-water probe. *J. Atmos. Oceanic Technol.,* **12,** 410–414.

——, A. J. Illingworth, A. J. Heymsfield, G. M. McFarquhar, K. A. Browning, and M. Gosset, 1995: The role of spaceborne millimeter-wave radar in the global monitoring of ice-cloud. *J. Appl. Meteor.,* **34,** 2346–2366.

Donovan, D. P., 2003: Ice-cloud effective particle size parameterization based on combined lidar, radar reflectivity, and mean Doppler velocity measurements. *J. Geophys. Res.,* **108,** 4573, doi:10.1029/2003JD003469.

——, and A. C. A. P. van Lammeren, 2001: Cloud effective particle size and water content profile retrievals using combined lidar and radar observations—1. Theory and examples. *J. Geophys. Res.,* **106,** 27 425–27 448.

Edwards, J. M., and A. Slingo, 1996: Studies with a flexible new radiation code—1. Choosing a configuration for a large scale model. *Quart. J. Roy. Meteor. Soc.,* **122,** 689–719.

Eloranta, E. W., 1998: A practical model for the calculation of multiply scattered lidar returns. *Appl. Opt.,* **37,** 2464–2472.

European Space Agency, 2001: EarthCARE—Earth Clouds, Aerosols and Radiation Explorer. ESA/ESTEC ESA SP-1257 (1)—The five candidate Earth Explorer Core Missions, 130 pp.

——, 2004: EarthCARE—Earth Clouds, Aerosols and Radiation Explorer. ESA/ESTEC ESA SP-1279(1)—The six candidate Earth Explorer Missions, 60 pp.

Field, P. R., 2000: Bimodal ice spectra in frontal clouds. *Quart. J. Roy. Meteor. Soc.,* **126,** 379–392.

Foot, J. S., 1988: Some observations of the optical properties of clouds—2. Cirrus. *Quart. J. Roy. Meteor. Soc.,* **114,** 145–164.

Francis, P. N., P. Hignett, and A. Macke, 1998: The retrieval of cirrus cloud properties from aircraft multi-spectral reflectance measurements during EUCREX'93. *Quart. J. Roy. Meteor. Soc.,* **124,** 1273–1291.

Hess, M., R. B. A. Koelemeijer, and P. Stammes, 1998: Scattering matrices of imperfect hexagonal ice crystals. *J. Quant. Spectrosc. Radiat. Transfer,* **60,** 301–308.

Heymsfield, A. J., and D. G. Baumgardner, 1985: Summary of workshop on processing 2-D probe data. *Bull. Amer. Meteor. Soc.,* **66,** 437–440.

Hogan, R. J., and A. J. Illingworth, 1999: The potential of spaceborne dual-wavelength radar to make global measurements of cirrus clouds. *J. Atmos. Oceanic Technol.,* **16,** 518–531.

——, and ——, 2003: Parameterizing ice cloud inhomogeneity and the overlap of inhomogeneities using cloud radar data. *J. Atmos. Sci.,* **60,** 756–767.

——, ——, and H. Sauvageot, 2000: Measuring crystal size in cirrus using 35- and 94-GHz radars. *J. Atmos. Oceanic Technol.,* **17,** 27–37.

——, P. N. Francis, H. Flentje, A. J. Illingworth, M. Quante, and J. Pelon, 2003: Characteristics of mixed-phase clouds—1. Lidar, radar and aircraft observations from CLARE'98. *Quart. J. Roy. Meteor. Soc.,* **129,** 2089–2116.

——, M. D. Behera, E. J. O'Connor, and A. J. Illingworth, 2004: Estimating the global distribution of supercooled liquid water clouds using spaceborne lidar. *Geophys. Res. Lett.,* **32,** L05106, doi:10.1029/2003GL018977.

——, M. P. Mittermaier, and A. J. Illingworth, 2006: The retrieval of ice water content from radar reflectivity factor and temperature and its use in evaluating a mesoscale model. *J. Appl. Meteor.,* in press.

Illingworth, A. J., and T. M. Blackman, 2002: The need to represent raindrop size spectra as normalized gamma distributions for the interpretation of polarization radar observations. *J. Appl. Meteor.,* **41,** 287–297.

Intrieri, J. M., G. L. Stephens, W. L. Eberhart, and T. Uttal, 1993: A method for determining cirrus cloud particle sizes using lidar and radar backscatter techniques. *J. Appl. Meteor.,* **32,** 1074–1082.

Klett, J. D., 1985: Lidar inversion with variable backscatter/extinction ratios. *Appl. Opt.,* **24,** 1638–1643.

Liou, K.-N., 1986: Influence of cirrus clouds on weather and climate processes: A global perspective. *Mon. Wea. Rev.,* **114,** 1167–1199.

Mace, G. G., K. Sassen, S. Kinne, and T. P. Ackerman, 1998: An examination of cirrus cloud characteristics using data from millimeter wave radar and lidar: The 24 April SUCCESS case study. *Geophys. Res. Lett.,* **25,** 1133–1136.

Matrosov, S. Y., A. V. Korolev, and A. J. Heymsfield, 2002: Profiling cloud ice mass and particle characteristic size from Doppler radar measurements. *J. Atmos. Oceanic Technol.,* **19,** 1003–1018.

McClatchey, R. A., R. W. Fenn, J. E. A. Selby, F. E. Volz, and J. S. Garing, 1972: Optical properties of the atmosphere. 3d ed. Air Force Cambridge Research Laboratories Rep. AFCRL72-0497, 108 pp.

McFarquhar, G. M., and A. J. Heymsfield, 1997: Parameterization of tropical cirrus ice crystal size distributions and implications for radiative transfer: Results from CEPEX. *J. Atmos. Sci.,* **54,** 2187–2200.

Mitchell, D. L., S. K. Chai, Y. Liu, A. J. Heymsfield, and Y. Dong,

1996a: Modeling cirrus clouds. Part I: Treatment of bimodal size spectra and case study analysis. *J. Atmos. Sci.,* **53,** 2952–2966.

——, A. Macke, and Y. Liu, 1996b: Modeling cirrus clouds. Part II: Treatment of radiative properties. *J. Atmos. Sci.,* **53,** 2967–2988.

O'Connor, E. J., R. J. Hogan, and A. J. Illingworth, 2005: Retrieving stratocumulus drizzle parameters using Doppler radar and lidar. *J. Appl. Meteor.,* **44,** 14–27.

Platt, C. M. R., 1981: Remote soundings of high clouds. III: Monte Carlo calculations of multiple-scattered lidar returns. *J. Atmos. Sci.,* **38,** 156–167.

Slingo, A., and H. M. Schrecker, 1982: On the shortwave radiative properties of stratiform water clouds. *Quart. J. Roy. Meteor. Soc.,* **108,** 407–426.

Stephens, G. L., 1978: Radiation profiles in extended water clouds. II: Parameterization schemes. *J. Atmos. Sci.,* **35,** 2123–2132.

——, and Coauthors, 2002: The CloudSat Mission and the A-Train. *Bull. Amer. Meteor. Soc.,* **83,** 1771–1790.

Testud, J., S. Oury, X. Dou, P. Ameyenc, and R. Black, 2001: The concept of normalized distribution to describe raindrop spectra: A tool for cloud physics and cloud remote sensing. *J. Appl. Meteor.,* **40,** 1118–1140.

Thomas, L., J. C. Cartwright, and D. P. Wareing, 1990: Lidar observations of the horizontal orientation of ice crystals in cirrus clouds. *Tellus,* **42B,** 211–216.

Tinel, C., 2002: Restitution des propriétés microphysiques et radiatives des nuages froids et mixtes à partir des données du système RALI (radar/lidar). Ph.D. thesis, 237 pp.

——, J. Testud, R. J. Hogan, A. Protat, J. Delanoe, and D. Bouniol, 2005: The retrieval of ice cloud properties from cloud radar and lidar synergy. *J. Appl. Meteor.,* **44,** 860–875.

Vaughan, J. M., N. J. Geddes, P. H. Flamant, and C. Flesia, 1998: Establishment of a backscatter coefficient and atmospheric database. DERA/EL/ISET/CR980129/1.0, ESA Contract 12510/97/NL/RE, 110 pp.

Wang, Z., and K. Sassen, 2002: Cirrus cloud microphysical property retrieval using lidar and radar measurements. Part I: Algorithm description and comparison with in situ data. *J. Appl. Meteor.,* **41,** 218–229.